The Influence of Peritectic Reaction/Transformation on Crack Susceptibility in the Continuous Casting of Steels

SAUD SALEEM, MICHAEL VYNNYCKY, and HASSE FREDRIKSSON

The work presented here examines the surface cracks that can form during the continuous casting of near peritectic steels due to the volume changes during the peritectic reaction/transformation. The investigated samples were collected during plant trials from two different steel grades. The role and mode of the peritectic reaction/transformation are found to depend on the composition of the alloy, resulting in different types of surface cracks. The effect of the local variation in the cooling rate on the formation of the different types of cracks present in each steel grade, which can be due, for example, to the formation of oscillation marks, is demonstrated. The enhanced severity of the surface and internal oxidation, both of which depend on the alloy composition and consequent peritectic reaction, is highlighted. Experimental and theoretical studies show that different types of surface cracks can occur in peritectic steels depending upon the alloy composition and cooling rate, both of which define the fraction of the remaining liquid upon completion of the peritectic reaction/transformation.

DOI: 10.1007/s11663-017-0926-8

I. INTRODUCTION

THE surface cracking of continuously cast steel has drawn the attention and focus of many researchers, since it affects the efficiency of the casting process. Continuous research has helped to understand the phenomenon of crack formation at the early stages of continuous casting (CC) and has improved the process quality considerably.[1–3] In earlier work,[1,4] Brimacombe *et al*. investigated the crack formation in different steel grades during continuous casting and explained the theory behind it. They related crack formation with the surface depressions, while the effect of melt stream impingement was found to cause the so-called white bands and structure changes. Harada *et al*.[2] investigated the role of the surface segregation in the formation and propagation of the cracks during CC and proposed a mechanism based upon these observations. Takeuchi *et al*.[3] observed transverse cracks under the oscillation mark (OM) depressions and along the austenite grain boundaries. Maehara *et al*.[5] considered the effect of local delay of solidification due to the uneven surface cooling on low-alloyed peritectic steels during continuous casting and suggested that the crack susceptibility will be largely accelerated by this mechanism.

Steels that undergo peritectic reaction and transformation complicate the CC process. Hypo-peritectic steels ($\underline{C} < 0.16$ wt pct) are particularly susceptible to crack formation.[4] The crack susceptibility of the initially formed shell increases due to the additional stresses and strains resulting from the fact that the primary and secondary solid phases have different densities.[6–10] Peritectic transformation that follows upon completion of the peritectic reaction generates high tensile strain and a contraction which can lead to crack formation in the initially solidified brittle material.[1,11–13] Fredriksson[14] utilized the method of unidirectional solidification to investigate the peritectic transformation in high-alloyed steels containing ferrite stabilizers. Based on his experimental results, he concluded that the peritectic temperature and extent of the peritectic transformation increase with increasing cooling rate. Moreover, at high cooling rates, the transformation occurred very rapidly without any diffusion of the alloying elements into the interior of the ferrite. Nassar and Fredriksson[15] performed many DTA experiments on low-alloy steels and observed a massive transformation of δ to γ, which they attributed to stress relief relaxation, since such a transformation rate cannot be explained by a diffusion-driven transformation.

The surface oxidation of the strand outside the mold is an inevitable phenomenon. An oxide skin forms on the surface of the strand due to the prolonged exposure of the surface to atmosphere at higher temperatures. Oxidation can extend beneath the surface along the grain boundaries and can cause cracks to grow inside the material.[16] The brittle oxidation layer at the grain boundary is highly prone to surface and subsurface crack initiation[17] during rolling or further deformation. The penetration of the oxide layer inside the material can be attributed to stress-accelerated grain boundary oxidation.[18] The coherent layer of the compound makes it impossible for the material to weld back at

SAUD SALEEM, MICHAEL VYNNYCKY, and HASSE FREDRIKSSON are with the KTH Royal Institute of Technology, Brinellvgen 23, SE-10044 Stockholm, Sweden. Contact e-mail: sauds@kth.se

Manuscript submitted March 4, 2016.
Article published online February 10, 2017.

higher temperature during the formation and nucleation of cracks.

In the present work, a detailed investigation of the surface and subsurface cracks formed during CC of peritectic steels has been undertaken. Samples taken at the surface of the steel strand have been examined by microscopic analysis restricted to the vicinity of the strand chill surface. The segregation behavior of the cracks has been analyzed with the aid of microprobe measurements. The possible effect of the peritectic transformation on the formation of the cracks is assessed with the help of a thermomechanical model. By combining experimental observations and computed results, an explanation for the different types of observed cracks is presented.

II. EXPERIMENTAL

Plant trials were performed on heats from two different companies. The cast from company A is a bloom with a rectangular section of 265 × 365 mm, while samples from a slab with a cross section of 290 × 1680 mm were obtained from company B. The mold from which the samples were taken, from company A, was a curved Sanicro 41 Cu-coated wall, oscillating in sinusoidal mode with constant stroke, with melt inlet through a submerged entry nozzle; the samples from company B were taken from a mold with a straight chromium-coated wall, oscillating in sinusoidal mode with fixed stroke. The casting conditions and material compositions are given in Tables I and II, respectively.

Samples having a length of 250 mm and a cross section of 10 × 10 mm were cut mechanically from the narrow face of the strand in order to avoid the possible effect of soft reduction and distortion in the as-cast outer contour of the chill surface. The oil and oxidized surface layer on the etched and unetched surfaces of samples were first removed by a wire metal brush to reveal the existing cast surface. The specimens were ground and polished by standard surface finish for micro-examinations. The specimens were then micro-etched with a solution of 4 to 9 g picric acid in 100 mL of H_2O. These were then cleaned in an ultrasonic cleaner by placement in a solution of (3 mL) HCl, (50 mL) water and (4 mL) 2 Butyne-1 diol, followed by a light polishing for 20 seconds.

The subsurface microstructure was photographed continuously through the entire length of the collected samples. The elemental analysis was performed using energy-dispersive X-ray spectroscopy (EDXS) method with JEOL scanning electron microscope. Some of the samples from heat 1 were selected for surface mapping of the microsegregation using microprobe analysis with a resolution of 1 μm × 1 μm. In order to investigate the extent of the crack into the material, samples from heat 2 were quenched in liquid nitrogen and hammered to fracture.

III. MODEL DESCRIPTION

A. *Thermal Model*

In the continuous casting of steels, melt enters in a vertical oscillating mold at a temperature above the liquidus of the alloy and starts to solidify next to the mold wall. In the simulations, however, the melt is considered to enter the mold region at the liquidus temperature; hence, the liquidus line will lie at the inlet of the mold, *i.e.*, $T = T_{liq}$ at $z = 0$. Heat flow can be described by the heat conduction in the thickness (x), transverse (y), and axial (z) directions and heat convection due to the bulk motion of the solidifying material. An internal heat generation source is normally added into the heat balance in order to incorporate the effect of latent heat of fusion due to the liquid to solid phase change. Casting geometries, especially for the initial solidifying strand inside the mold, are slender. The resistance to the heat conduction along the x-direction of the strand is much smaller than that in the y- and z-directions. Thus, the heat balance is given by

$$\rho\left\{C_p + \Delta H_f \frac{df_l}{dT}\right\} v\frac{\partial T}{\partial z} = k\frac{\partial^2 T}{\partial x^2}; \qquad [1]$$

the physical quantities in Eq. [1] are given in Tables I and III. Although Eq. [1] is, strictly speaking, better suited to the modeling of slab casting rather than to that of blooms casting, we shall nevertheless use this form in this paper, since the inclusion of the additional temperature derivatives with respect to y on the right-hand side would not introduce any new significant physics that is of relevance to our general discussion of peritectic reactions/transformations; moreover, the simplification means that the subsequent numerical calculation is relatively straightforward. For the case of solidification with some diffusion of the solute into the solid phase, the following constitutive relation between liquid fraction, f_l, and temperature can be used:

$$f_l = 1 - \frac{T_{liq} - T - \frac{2}{\pi}(T_{liq} - T_{sol})\left(1 - \cos\left(\frac{\pi}{2}\left(\frac{T - T_{liq}}{T_{sol} - T_{liq}}\right)\right)\right)}{(T_{liq} - T_{sol})\left(1 - \frac{2}{\pi}\right)}. \qquad [2]$$

Table I. Casting Parameters for the Studied Heats

Parameters	Company A (Heat 1)	Company B (Heat 2)
Mold sinusoidal mode (f)	176 cycle/min	95 cycle/min
Stroke (s)	±2 mm	±2.9 mm
Casting speed (v)	0.8 m/min	0.78 m/min

Table II. Composition Analysis of the Studied Heats

Heat	C	Si	Mn	Cr	Ni	Mo
1	0.231	0.30	0.67	1.28	2.88	0.24
2	0.16	0.43	1.52	—	—	—

Table III. Parameters Used for the Heat Transfer Model

Symbol	Value	Description
T_{liq}	1773 K (1499.85 °C)	liquidus temperature
T_{sol}	1713 K (1439.85 °C)	solidus temperature
T_p	1766 K (1492.85 °C)	peritectic temperature
T_f	1746 K (1472.85 °C)	end of peritectic transformation
k	33 W/m K	thermal conductivity
C_p	700 J/kg K	specific heat
ΔH_f	262 kJ/kg	heat of fusion
ρ_δ	7876 kg/m^3	ferrite density
ρ_γ	8100 kg/m^3	austenite density
T_{00}	298.15 K (25 °C)	ambient temperature

The descriptions and the selected values of the physical constants are given in Table III. The reason for the selected functional form of f_l is its capability to better describe the behavior of multicomponent systems.[19,20] The selection of an alternative functional form of f_l will result in the redistribution of the temperature field in the model domain. The volumetric strain depends on the temperature difference instead of the temperature gradients. Hence, any other form of f_l will redistribute the strain without affecting the magnitude at a particular temperature.

There are two boundary conditions for the heat transfer model in order to find the solution without calculating the phase transformation boundaries explicitly. In order to see the complete model details where one can compute the required location of the boundaries simultaneously, the reader is referred to earlier work.[21,22]

The first boundary condition is expressed as

$$z \geq 0,\ x = 0 : -k\frac{\partial T}{\partial x} = h(T - T_{00}),$$

where h is the heat transfer coefficient in W/m^{2}K, which could be a function of z, or time, t. For the steady-state condition, the distance translated by a point in space and corresponding time can be found by substituting $z = vt$. The other boundary condition is the axis of symmetry at the centerline of the cast:

$$z \geq 0,\ x = \frac{W}{2} : -k\frac{\partial T}{\partial x} = 0,$$

where W is the width of the casting in the x-direction.

B. *Mechanical Model*

During cooling, the solidifying shell and coherent mush will be strained due to thermal contraction and phase change.[23] The total strain in the system, ε_{tot}, is given by

$$\varepsilon_{tot} = \varepsilon_{th} + \varepsilon_m + \varepsilon_{ph}, \quad [3]$$

where $\varepsilon_{th}, \varepsilon_m,$ and ε_{ph} are thermal, mechanical, and phase change strains, respectively. The thermal strain results due to the continuous decrease in the temperature of system and the contraction of the casting. The mechanical strain arises due to the fact that neighboring points in the cast have different thermal strains due to different cooling rates.

The difference in densities between austenite and ferrite develops stress and strain over the interface and results in the strain due to phase change. Due to the larger molar volume of δ-phase, it has to be compressed at and close to the δ/γ interface in order to match the lower molar volume of γ-phase. The hydrostatic strain then can be described by the density difference and fraction of the δ-phase transformed to γ-phase with the relation

$$\varepsilon_{ph} = \frac{1}{3}\beta \int_{Y_p}^{Y_f} \frac{\partial f'}{\partial z} dz, \quad [4]$$

where β represents the fractional change in density because of the ferrite to austenite transformation and is defined as $\beta = (\rho_\delta - \rho_\gamma)/\rho_\delta$, whereas the values of the densities for ferrite, ρ_δ, and austenite, ρ_γ, are given in Table III. Y_p is the position of the peritectic isotherm and Y_f is the position of the front at which transformation finishes, and will be defined by the peritectic temperature range. f' represents the fraction of austenite formed by the transformation from ferrite. The $\delta \rightarrow \gamma$ transformation is normally described by the diffusion of the alloying elements. In the case of the low-alloyed carbon steel, the growth of the austenite phase can be considered to be controlled by carbon diffusion.[10] For multicomponent systems such as the investigated heats which contain Ni and Cr in addition to carbon, a more complex diffusion model has to be considered in order to describe the peritectic transformation.[11,14] The model should be able to describe multiple diffusion mechanisms of each element

simultaneously and to predict the resultant growth rate of the transformed austenitic phase. However, such a sophisticated modeling approach is beyond the scope of the current study, which is mostly based on the experimental investigations. In order to simplify the problem, the relation given earlier in Eq. [2] is utilized to describe the peritectic transformation of the multicomponent system as well; furthermore, the temperatures T_{liq} and T_{sol} in Eq. [2] will be replaced by T_p and T_f, respectively, where T_p is the peritectic temperature and T_f is the temperature at which the transformation finishes. The calculated fraction of $\delta \rightarrow \gamma$ transformation is then multiplied by the ferrite fraction present at the start of the peritectic transformation in order to find f^{γ}. For the early stage of solidification and during the peritectic transformation, the thermal and mechanical strains are much smaller than the strain due to phase change and are neglected in the following analysis.

IV. RESULTS

A. *Experimental Results*

Different types of cracks were observed in the studied heats. These cracks can be categorized on the basis of whether the fracture plane is segregated or non-segregated. As will be explained in the later sections, this will help to describe the effect of the composition and cooling rate on the formation of different types of crack. Heat 1 shows the presence of both types of crack, while in heat 2 only non-segregated cracks are observed.

B. *Segregated Cracks (Heat 1)*

The observed cracks in heat 1 can be further characterized as segregated and non-segregated cracks. Figure 2(a) shows the observed cracks where the fracture plane shows high segregation of alloying elements. The segregation bands are observed to cross the chunk of the dendrites and fracture the dendrites in the longitudinal direction (Figure 2(b)). The primary shell cracks at around a distance of 1.5 to 2 mm from the chill surface.

The observed segregation bands are not the result of the melt stream impingement which can cause the structure change and hot spots.[1] The structure change due to impingement does not happen before the shell solidifies to a thickness of 5 mm, as is observed in the microstructure. Hence, the observed bands are not a consequence of the melt stream.

A careful metallographic investigation showed that such bands were mostly observed under the depression of each oscillation mark. A possible reason for this was that these regions solidified to ferrite and transformed to austenite by a peritectic reaction. In the other regions, the solidification starts with a primary precipitation of austenite which then transforms to ferrite. Figure 3 shows a patch of the sample taken from the slice at the center of the strand, as shown in Figure 1. The distance between the consecutive bands is close to the average measured pitch of the marks. This shows the possibility that the formation of the bands might be related to, or enhanced by, the formation of OMs probably due to a lower cooling rate in these regions. OM2 shown in Figure 3 shows a further splitting of the primary shell by the formation of an additional band and shows the stacking of multiple fracture planes.

The microprobe analysis of the segregated fracture plane for the outlined areas, A1 and A2 in Figure 2, is presented in Figure 4. The average composition in the areas marked as A1–A5 in Figure 4 is presented in Table IV, while the average composition of the areas marked as A6–A8 in Figure 4 is shown in Table V. All the elements show positive segregation except Ni, which shows negative segregation. Mo shows highest segregation with a segregation index (S) of 1.56 in A2.

C. *Elemental Mapping*

Area A2, which is at the chill surface, shows higher Cr content and lower Mn content as compared to A1, which is further from the surface. The elemental maps show localized higher segregation regions of Mn, which could be MnS inclusions (Figure 5). The observed peaks for Cr in Figure 6 show the possible presence of carbides.

D. *Non-segregated Cracks (Heat 1)*

Some of the domains were observed at the etched surface of heat 1. These domains were large enough to be visible to the naked eye, and were formed by the intra-granular cracking where cracks crossed the chunk of the dendrites. A magnified view of the domains is presented in Figure 7. The dendritic structure inside the domain is coarser and is clearly different from the surrounding more refined and normally solidified microstructure. The domains are formed by the cracks in the primary solidified columnar grains. The formed cracks do not show any segregation and are different from the cracks mentioned earlier. These cracks were observed in the regions between and under relatively shallower depressions. The formation of these cracks under high cooling is very likely since the distance of the strand chill surface from the mold cold face is relatively smaller for the formation of the cracks. A refined domain-like structure shown in Figure 7 suggests the possibility of the presence of multiple nucleation sites in the crack-formed regions. The material due to the presence of the nucleation sites and higher cooling rates, in the non-segregated cracked zone, might have solidified to delta ferrite primarily followed by the transformation to austenite, while the surrounding material solidified to austenite directly.

E. *Surface Oxidation and Non-segregated Cracks (Heat 2)*

An externally intact oxide skin of thickness 50 to 100 μm was observed for both steel grades. Figure 8 shows the oxide wedge formed at the chill surface of heat 1. The composition analysis of the inside notch in Figure 8 shows the presence of complex oxides of the form CrO-Fe. The root of the penetrating oxide layer is

detached from the material matrix. This shows the possibility that the oxide layer growth stopped before the oxidation of the cracked internal surface area, especially at the root.

The oxidation of the grain boundaries can be observed throughout the span for heat 2 (Figure 9).

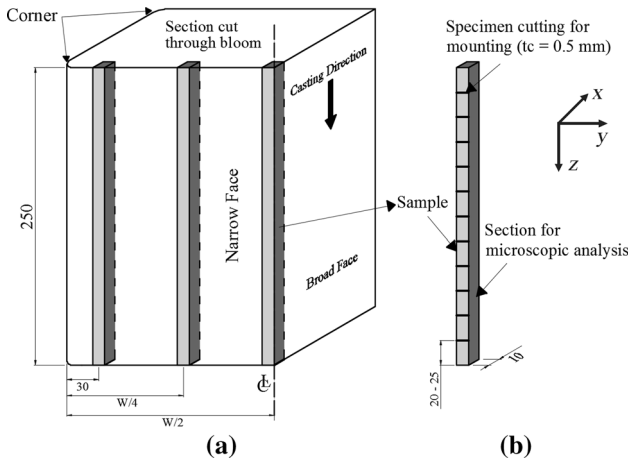

Fig. 1—(*a*) Schematic showing the positions of the samples. (*b*) Cutting of longer samples to laboratory-scale specimen (tc = cutting disk thickness).

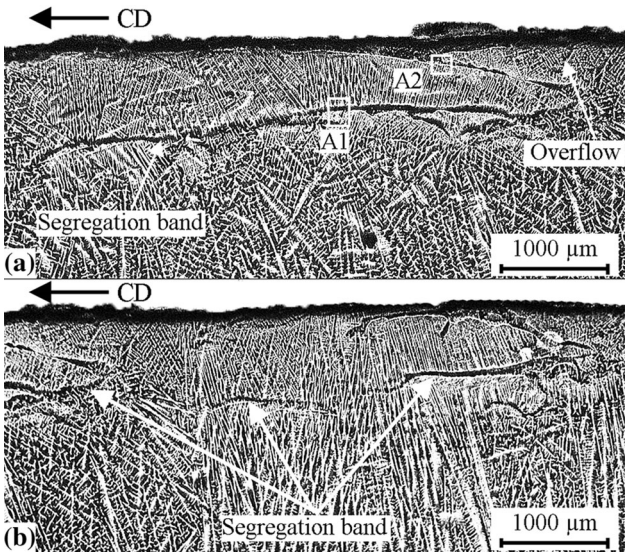

Fig. 2—(*a*) Observed bands under OM show segregation plan. (*b*) Transverse cracking of the dendrites and filling of cracks with inter-dendritic liquid to form segregation bands.

The thickening of the grain boundaries occurs due to the extent of the surface oxidation along and across the grain boundary. The oxidation layer penetrates to a greater depth in heat 2 as compared to heat 1 (up to 1 mm).

Mold flux (slag) is entrapped in the surface oxidation layer. The composition analysis presented in the coming sections will confirm the observations. A layer with darker appearance can be observed inside the material next to the outer oxidized surface layer. The layer could have possibly formed by subsurface oxidation. Figure 9 also shows a closer view of the surface where small oxide particles can be seen inside the matrix. This is some type of internal oxidation due to a faster diffusion of oxygen in the oxides.

The layer also causes the propagation of the cracks in heat 2. To verify this, some of the samples were quenched in liquid nitrogen and hammered to fracture. Figure 10 shows the SEM image of the fracture surface. The propagation of the crack along the grain boundary is evident. The cracked section also shows the chill surface and subsurface oxidized layer.

The grain boundaries under the depressions, however, show thick and adverse oxidation and formation of the cracks as shown in Figure 11. Figure 12 shows the point analysis performed with SEM equipped with EDS for the outlined area in Figure 11. Point 5 in Figures 12(a) and (b) shows higher oxygen content, and hence the presence of the oxidation layer. Point 6, however, shows Ca, F, and Si, and also higher oxygen content (Figures 12(a) and (b)). Since Ca and F are absent in the material and present in the slag, the darker particles must be the entrapped mold slag drawn along the grain boundary by the oxidation layer. The considerable increase in the Si concentration shows the possibility of SiO_2, which is present in abundance in the mold powder.

Small oxide particles can be seen next to the oxide layer. The composition analysis for the points marked in Figure 12(a) is presented in Table VI. Point a, which is taken in the material matrix, shows the absence of O, while the rest of the particle shows the presence of Si and O. The higher atomic percentage of O shows the possibility of more than Si oxides. There exists the possibility for the precipitation of Fe and Mn oxides.

Figure 13 shows the precipitation of the oxides ahead of the tip of the oxidation layer which is marked in Figure 11. The particle can promote the penetration of the oxide layer and crack formation over time at higher temperatures. The highest oxygen contents were measured for the particles close to the tip (Table VII).

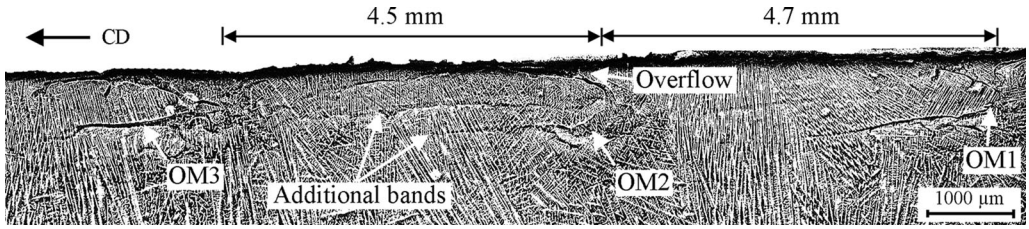

Fig. 3—Serial formation of segregation bands under OMs with inter-distance equal to the average pitch.

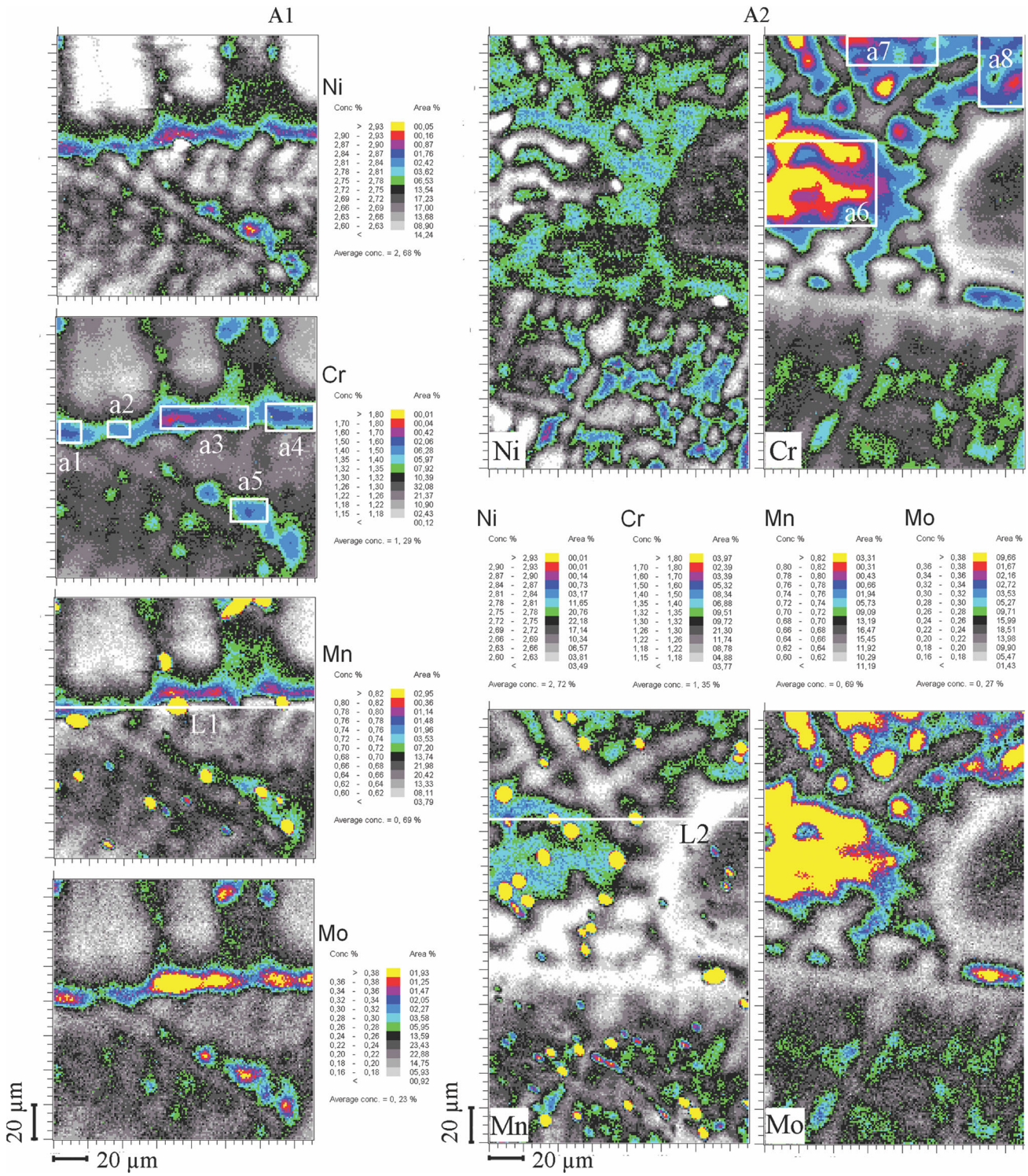

Fig. 4—Microprobe measurements for the element mapping of the areas outlined as A1 and A2 in Fig. 2(a).

Particles relatively bigger in size show the presence of Ca and Na (point 7), and hence the possible presence of the mold flux. The comparison of the measurements across (Table VI) and along (Table VII) the oxidation layer shows higher oxygen content along the layer, indicating the rapid transverse growth of the oxide layer.

F. *Simulation Results*

In what follows, all the simulation results are for heat 1 only; the reason why no simulations were carried out for heat 2 is explained later. The heat flux profile computed for the model is presented in Figure 14. The values of the heat flux are close to the ones reported

Table IV. Average Composition of the Elements for the Marked Areas in Fig. 4

Area	Si	Mn	C	Mo	Ni	Cr
A1	0.36	0.97	0.20	0.32	2.81	1.45
A2	0.36	0.70	0.20	0.29	2.79	1.41
A3	0.37	1.00	0.31	0.36	2.78	1.48
A4	0.37	0.78	0.27	0.34	2.80	1.46
A5	0.36	0.75	0.29	0.32	2.81	1.42
Average ($\bar{C}$), wt pct	0.36	0.84	0.25	0.33	2.80	1.44
Nominal (C_0), wt pct	0.30	0.67	0.23	0.24	2.88	1.28

Table V. Average Composition of the Elements for the Marked Areas in Fig. 4

Area	Si	Mn	C	Mo	Ni	Cr
A6	0.37	0.83	0.25	0.45	2.69	1.73
A7	0.35	0.72	0.20	0.35	2.71	1.51
A8	0.36	0.71	0.21	0.32	2.72	1.50
Average ($\bar{C}$), wt pct	0.36	0.75	0.22	0.37	2.71	1.58
Nominal (C_0), wt pct	0.30	0.67	0.23	0.24	2.88	1.28
$S = {}^{C}/_{C_0}$	1.20	1.12	0.95	1.56	0.94	1.23

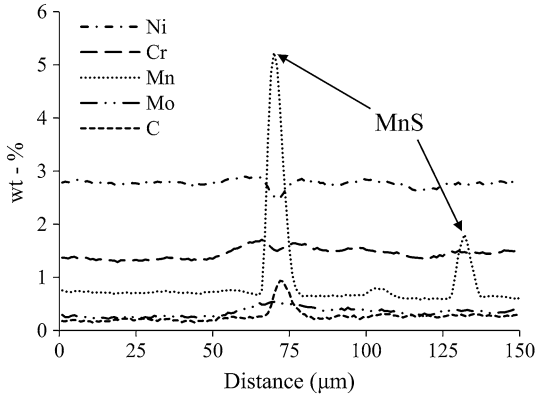

Fig. 5—Composition measurements for line L1, marked in Fig. 4, showing the presence of MnS particles.

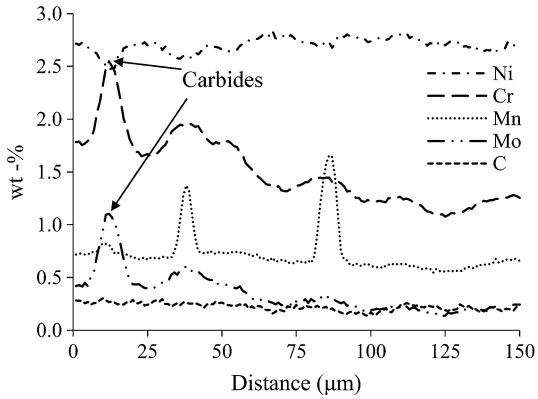

Fig. 6—Composition measurements for line L2, marked in Fig. 4, showing the possible presence of carbides.

earlier.[24] The positions of the calculated fronts for the early stage of the solidification are given in Figure 15.

The reaction starts at temperature T_p, whereas Y_p shows the position of the front in the mold. Y_f is the position at which peritectic transformation finishes. The calculation presented in Figure 15 for heat 1 shows that the transformation finishes much earlier than the final solidification. Some of the liquid is left after the ferrite to austenite transformation. This will reduce the mechanical strains in the system without affecting the phase transformation strain that occurs over the ferrite/austenite interface. This will also reduce the stresses that develop in the shell due to the larger incoherent region during the peritectic transformation. The strain at the interface can cause the nucleation of the cracks which can grow once the shell attains coherency.

Hot ductility tests performed by Hansson[13] on a steel with the same composition as that of heat 1 showed that the material is very brittle in the peritectic transformation range. A small amount of strain can result in the formation of cracks, since the material does not attain any ductility unless it is below the solidus temperature. In the present analysis, however, the crack is deemed to have formed when the total strain exceeds 0.2 pct; the location of the front where the total strain equals 0.2 pct is shown in Figure 15. Figure 16 shows the calculated strain as a function of temperature at the chill surface of the strand and shows the possibility for the formation of the crack.

Lower C and higher Si content in heat 2 suggest that it has solidified mostly or completely to ferrite before the start of peritectic reaction. It then follows the solid-state transformation without the presence of the liquid film in between the ferrite grains.

V. DISCUSSION

The two different types of cracks, segregated and non-segregated, are a result of the peritectic reaction/transformation. The solidification of the two steels starts with a primary precipitation of ferrite, followed by peritectic reactions resulting in austenite. Some liquid

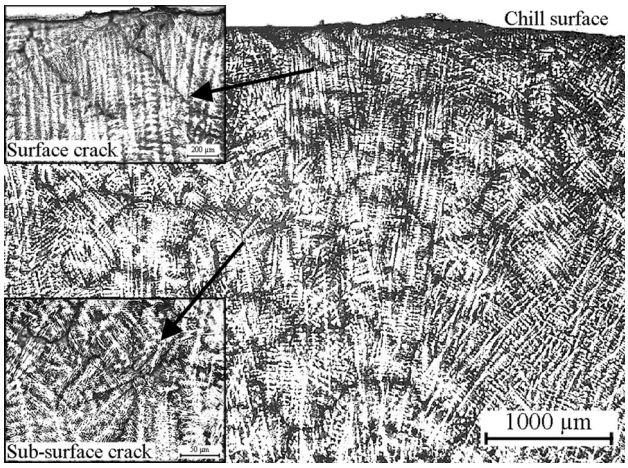

Fig. 7—Formation of the surface and subsurface cracks in a domain-like structure across the primary dendrites.

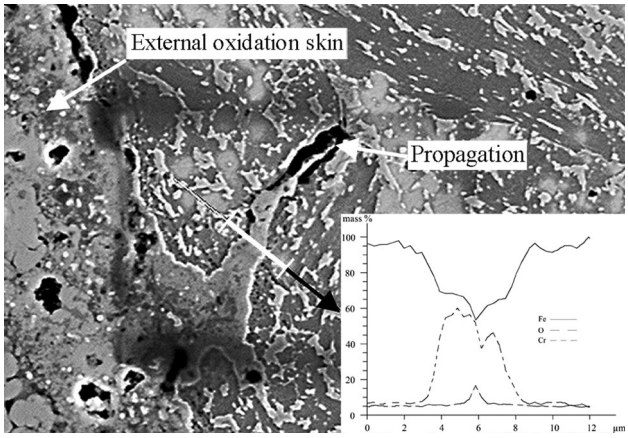

Fig. 8—Formation and propagation of the oxide skin at the chill surface of the heat 1.

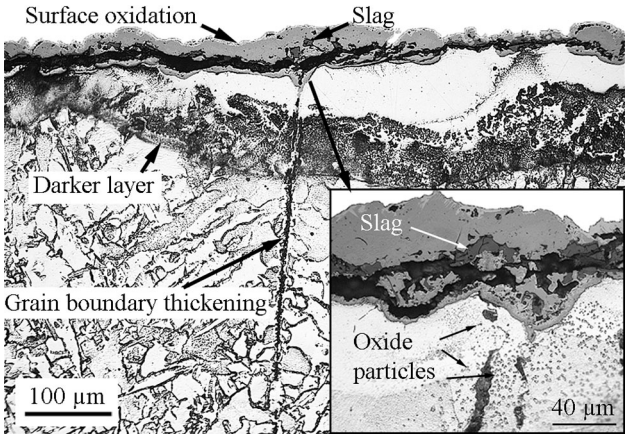

Fig. 9—Grain boundary oxidation outside the OM span in heat 2. Surface and subsurface oxidation with entrapped mold slag.

might remain, depending on the composition of the steel grades. The ferrite has a lower density than austenite, and this results in phase transformation strains and stresses during the peritectic reaction/transformation.

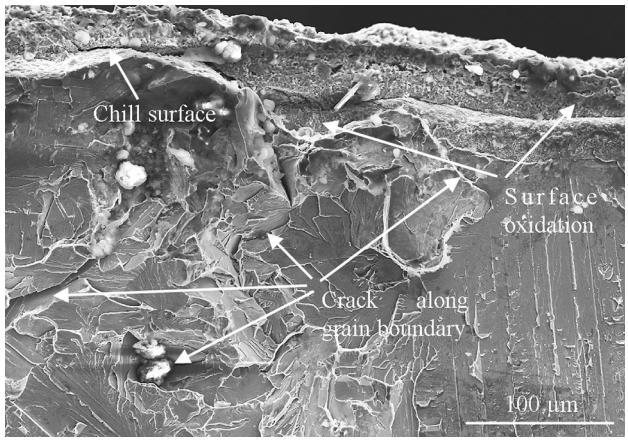

Fig. 10—Inter-granular cracks at fractured cross section close to the chill surface of cast from heat 2.

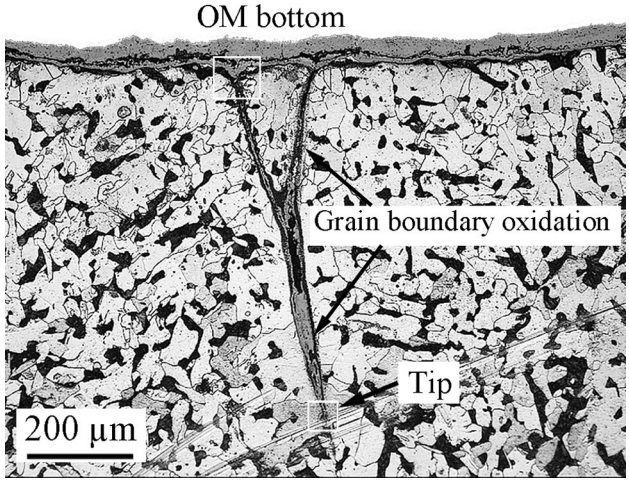

Fig. 11—Growth and thickening of the grain boundary oxidation at the bottom of the OM for heat 2.

The microstructure in the two cases suggests that the peritectic reaction/transformation occurs in a diffusionless manner. This type of transformation is very common and has been discussed and presented in a series of investigations by Fredriksson *et al.*[14] The transformation occurs by the growth of a front which is controlled by the strain relaxation. The strain will be relatively large, as shown by the simulation results, and the steels are very susceptible to crack formation at higher temperatures. Cracks are formed preferentially at the grain boundaries.

Heat 1 has lower Si and higher C and Ni content than heat 2. Due to alloying content, some liquid will be left when all the ferrite has transformed to austenite, as can be seen from the simulation results as well. The liquid film will avoid the formation of inter-granular cracks. However, the boundaries between ferrite and austenite grains or the phase boundary ferrite/austenite are highly susceptible to cracks due to phase change strain. The cracks formed as a result of the phase change strain for heat 1 can be filled with the remaining liquid left after the ferrite to austenite transformation. The composition

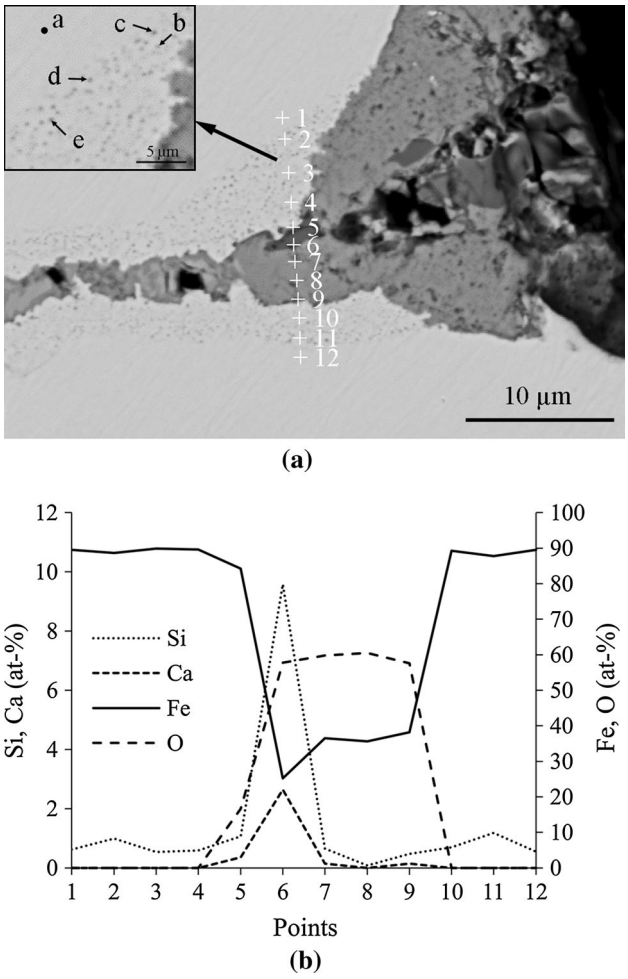

Fig. 12—(*a*) Precipitation of oxide particles next to the inter-granular oxidation. (*b*) Point EDS analysis shows mold slag entrapped in oxide layer formed in heat 2.

Table VI. Composition of the Oxides Particles Marked in Fig. 12(a)

Point	O (At. Pct)	Si (At. Pct)
a	—	0.7
b	10.4	1.5
c	12.8	2.0
d	12.9	2.1
e	13.5	2.5

of the liquid will be given by the austenite/liquid equilibrium line. The microprobe measurement shows the positive segregation of the elements at the fracture plane, which indicates that the cracks are filled with the enriched liquid during the solidification. A possible reason for the formation of segregated cracks under oscillation mark depressions could be the increased heat transfer especially during the negative strip period.[25]

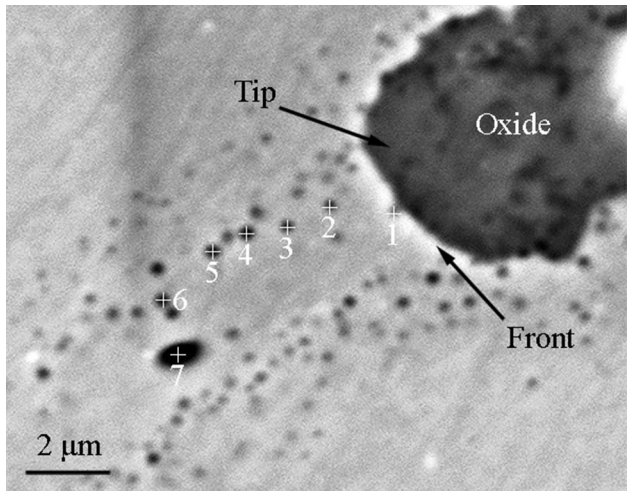

Fig. 13—Precipitation of oxide particles ahead of the oxidation layer tip marked in Fig. 11.

The increased heat transfer can promote the growth rate of the transformation and results in additional stresses in the material.

The non-segregated cracks in heat 1 are observed for the regions closer to the hot face of the mold, and Figure 7 shows the result of the alternative precipitation of the austenite and delta-ferrite phases. The driving force for the crack formation is, however, still the volume change due to the density difference between ferrite and austenite. The austenite precipitation is promoted due to the higher cooling rates, segregation, and precipitation of the nuclei, which act as nucleation sites. This statement is in accord with the earlier experimental and theoretical work done to investigate the effect of cooling rate and composition on the formation of the primary ferrite.[26] At the same time, higher cooling rate reduces the time for the solidification of the interdendritic liquid. However, the peritectic transformation is a diffusion-controlled phenomenon. Due to the higher cooling rates, the interdendritic liquid will solidify earlier than the peritectic strain reaches the critical value. This will result in the formation of the cracks which are not filled with remaining interdendritic liquid and are non-segregated.

Heat 2 solidified completely to ferrite before the transformation to austenite due to the lower carbon and higher Si content, as compared to heat 1. Due to the purely solid-state transformation, cracks are formed at the grain boundaries in heat 2. The cracks continue to grow due to the stress-accelerated grain boundary oxidation. The presence of the oxide particles close to the oxide layer shows the occurrence of the internal oxidation. This is a consequence of a very high diffusion rate of oxygen in the oxides and results in self-propagation of the crack. The diffusion rate of oxygen is increased due to the composition of the oxides. The oxidized brittle material is prone to cracking due to the thermal stresses that result from the continuous cooling

Table VII. Composition Measurements of the Particles Marked in Fig. 13

Point	C	O	Na	Al	Si	Ca	Mn	Fe
1	5.3	31.8	—	—	1.8	—	3.2	57.8
2	5.8	15.5	—	—	4.4	—	2.0	72.3
3	5.6	15.1	—	—	4.4	—	1.8	73.1
4	5.5	19.5	—	—	5.7	—	3.0	66.3
5	5.6	20.5	—	—	5.5	—	2.9	65.6
6	6.0	23.1	—	—	6.2	—	3.5	61.2
7	2.5	46.1	1.8	1.5	13.6	3.0	3.3	28.2

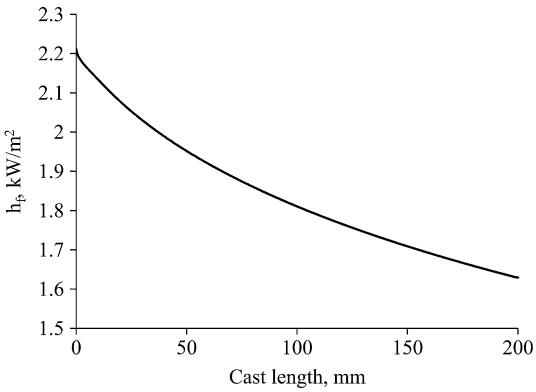

Fig. 14—Computed heat flux at the chill surface of the cast.

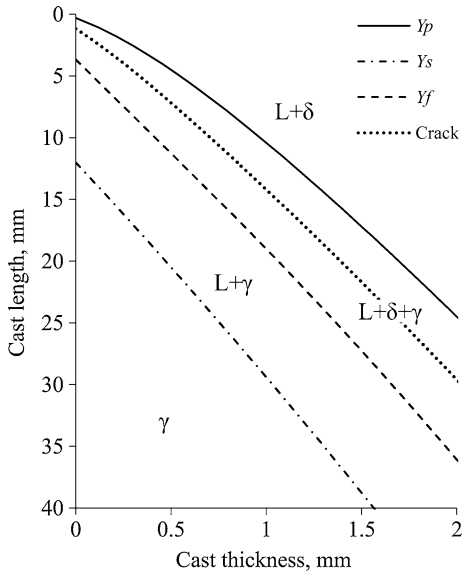

Fig. 15—Calculated position of different fronts during the peritectic solidification of heat 1 with higher C content.

of the material. The propagating cracked surface will be oxidized to a further extent, as shown in Figures 9 and 11.

VI. CONCLUSION

The strain caused by the peritectic reaction/transformation during the continuous casting of peritectic steel

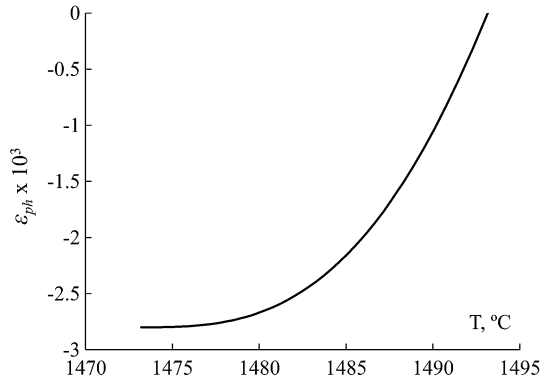

Fig. 16—Computed phase change strain due to peritectic reaction/transformation at the chill surface of heat 1.

makes the cast susceptible to cracking. Steel composition plays an important role in defining the type of the crack. Based upon the remaining volume fraction of the liquid after the peritectic reaction/transformation, inter- or intra-granular cracks can be formed. The oxidation of the surface can promote the crack growth and cause the crack to thicken and the possible embrittlement of the surrounding material due to the precipitation of the oxides.

ACKNOWLEDGMENTS

The authors wish to thank the Swedish Energy Agency (Energimyndigheten) for the provision of financial support. Useful discussions with Dr. Bo Rogberg are gratefully acknowledged. The authors also would like to thank Axel Jutner for his help to prepare some of the samples for the metallographic analysis.

OPEN ACCESS

REFERENCES

1. J.K. Brimacombe, F. Weinberg, and E.B. Hawbolt: *Metall. Trans. B*, 1979, vol. 10B, pp. 279–92.
2. S. Harada, S. Tanaka, H. Misumi, S. Mizoguchi, and S. Horiguchi: *ISIJ Int.*, 1990, vol. 30, pp. 310–16.
3. E. Takeuchi and J.K. Brimacombe: *Metall. Trans. B*, 1985, vol. 16B, pp. 605–25.
4. J.K. Brimacombe and K. Sorimachi: *Metall. Trans. B*, 1977, vol. 8B, pp. 489–505.
5. Y. Maehara, K. Yasumoto, Y. Sugitani, and K. Gunji: *Trans. Iron. Steel Inst. Jpn.*, 1985, vol. 25, pp. 1045–52.
6. J. Miettinen: *Metall. Trans. B*, 1997, vol. 28B, pp. 281–97.
7. J.O. Kristiansson: *J. Thermal Stresses*, 1982, vol. 5, pp. 315–30.
8. M. El-Bealy and H. Fredriksson: *Metall. Trans. B*, 1996, vol. 27B, pp. 999–1014.
9. A. Jablonka, K. Harste, and K. Schwerdtfeger: *Steel Res.*, 1991, vol. 62, pp. 24–33.
10. J. Konishi, M. Militzer, I.V. Samarasekera, and J.K. Brimacombe: *Metall. Trans. B*, 2002, vol. 33B, pp. 413–23.
11. J. Zou and A.A. Tseng: *Metall. Trans. A*, 1992, vol. 23A, pp. 457–67.
12. J. Miettinen: *Scand. J. Metall.*, 1993, vol. 22, pp. 317–24.
13. K. Hansson: PhD Dissertation, 2001, Royal Institute of Technology (KTH), Stockholm, Sweden.
14. H. Fredriksson: *Met. Sci.*, 1976, vol. 10, pp. 77–86.
15. H. Nassar and H. Fredriksson: *Metall. Trans. A*, 2010, vol. 41, pp. 2776–83.
16. C.J. McMahon and L.F. Coffin: *Metall. Trans.*, 1970, vol. 1, pp. 3443–50.
17. R.H. Bricknell and D.A. Woodford: *Metall. Trans. A*, 1981, vol. 12A, pp. 1673–80.
18. D.R. Muzyka, C.R. Whitney, and D.K. Schlosser: *J. Met.*, 1975, vol. 27, pp. 11–15.
19. B. Rogberg: *Scand. J. Metall.*, 1993, vol. 12, pp. 51–66.
20. S. Saleem, M. Vynnycky, and H. Fredriksson: *Adv. Sci. and Eng. of Casting Solidification*, 2015, pp. 15–22.
21. M. Vynnycky: *Proc. R. Soc. A*, 2009, vol. 465, pp. 1617–44.
22. M. Vynnycky, S. Saleem: *Appl. Math. Comp.*, 2014 (submitted).
23. M.O. El-Bealy: *Metall. Trans. B*, 2011, vol. 42, pp. 1280–96.
24. R.B. Mahapatra, J.K. Brimacombe, and I.V. Samarasekera: *Metall. Trans. B*, 1991, vol. 22B, pp. 875–88.
25. A. Badri, T.T. Natarajan, C.C. Snyder, K.D. Powers, F.J. Mannion, M. Byrne, and A.W. Cramb: *Metall. Trans. B*, 2005, vol. 36B, pp. 373–83.
26. H. Fredriksson, in: ASM Handbook, vol 15 Casting, D.M. Stefanescu ed., ASM International, Ohio, 1992, p. 125.